Martinez Garzon, P., Vavryčuk, V., Kwiatek, G., Bohnhoff, M. (2016): Sensitivity of stress inversion of focal mechanisms to pore pressure changes. - *Geophysical Research Letters*, *43*, 16, pp. 8441—8450.

DOI: http://doi.org/10.1002/2016GL070145

AGU PUBLICATIONS

Geophysical Research Letters

RESEARCH LETTER
10.1002/2016GL070145

Key Points:
- We analyze the stress inversion performance under different stress states using synthetic tests with varying pore pressure
- Stress ratio R changes and pore pressure are negatively correlated when $R < 0.6$
- This correlation holds for all stress regimes and is confirmed using data from fluid-induced seismicity and corresponding injection rates

Supporting Information:
- Supporting Information S1

Correspondence to:
P. Martínez-Garzón,
patricia@gfz-potsdam.de

Citation:
Martínez-Garzón, P., V. Vavryčuk, G. Kwiatek, and M. Bohnhoff (2016), Sensitivity of stress inversion of focal mechanisms to pore pressure changes, *Geophys. Res. Lett.*, *43*, 8441–8450, doi:10.1002/2016GL070145.

Received 22 JUN 2016
Accepted 1 AUG 2016
Accepted article online 8 AUG 2016
Published online 24 AUG 2016

The copyright line for this article was changed on 11 OCT 2016 after original online publication.

Sensitivity of stress inversion of focal mechanisms to pore pressure changes

Patricia Martínez-Garzón[1], Václav Vavryčuk[2], Grzegorz Kwiatek[1], and Marco Bohnhoff[1,3]

[1]Helmholtz Centre Potsdam GFZ German Research Centre for Geosciences, Potsdam, Germany, [2]Institute of Geophysics, Czech Academy of Sciences, Prague, Czech Republic, [3]Institute of Geological Sciences, Free University Berlin, Berlin, Germany

Abstract We investigate the sensitivity of stress inversion from focal mechanisms to pore pressure changes. Synthetic tests reveal that pore pressure variations can cause apparent changes in the retrieved stress ratio R relating the magnitude of the intermediate principal stress with respect to the maximum and minimum principal stresses. Pore pressure and retrieved R are negatively correlated when R is low ($R < 0.6$). The spurious variations in retrieved R are suppressed when $R > 0.6$. This observation is independent of faulting style, and it may be related to different performance of the fault plane selection criterion and variability in orientation of activated faults under different pore pressures. Our findings from synthetic data are supported by results obtained from induced seismicity at The Geysers geothermal field. Therefore, the retrieved stress ratio variations can be utilized for monitoring pore pressure changes at seismogenic depth in stress domains with overall low R.

1. Introduction

Stress field characterization contributes to identifying deformation zones and tectonically active structures at both local and regional scales. At shallow depth, in situ stress orientations can be recovered from borehole breakouts [e.g., *Hickman and Zoback*, 2004]. The magnitude of the vertical stress can be estimated using density logs and the minimum compressive stress σ_3 can be estimated, e.g., from leak-off tests. However, the depth range for in situ stress measurements is limited to several kilometers only [e.g., *Brudy et al.*, 1997]. Consequently, at greater depths the stress field orientation can only be inferred from earthquake focal mechanisms [e.g., *Zoback*, 1992]. The stress field orientation may be recovered with varying resolution depending on the amount of seismicity available, the focal mechanism uncertainties, and fault plane variability [e.g., *Hardebeck and Hauksson*, 2001; *Bohnhoff et al.*, 2004; *Vavryčuk*, 2015]. However, the absence of seismicity does not necessarily mean that the crust is not critically stressed.

The fluid saturation of rocks increases the pore pressure compared to the surrounding brittle crust and results in a reduction of the effective normal stress of nearby fractures. The presence of fluids at high pressures was reported at several segments of the San Andreas Fault based on observations of different stress orientations near the fault trace compared to the far field [*Hardebeck and Hauksson*, 1999]. The pore fluid pressure has also been suggested to play an important role in unlocking fault patches in the Nazca subduction interface resulting in the M_w 8.8 Chile earthquake [*Moreno et al.*, 2014]. Additionally, the pore pressure is coupled in poroelastic media with stress field, e.g., through fluid diffusion over long-time scales [e.g., *Townend and Zoback*, 2000] or by shear strain accumulation near active faults at shorter time scales [*Barbour*, 2015], and thus, it may locally modify the stress regime [*Segall and Fitzgerald*, 1998; *Altmann et al.*, 2014]. Stress changes related to fluids are highlighted in fluid-induced seismicity, where injection and production activities modify the pore pressure in the vicinity of the wells [e.g., *Terakawa et al.*, 2012; *Martínez-Garzón et al.*, 2013; *Schoenball et al.*, 2014]. Interestingly, changes in the relative magnitudes of the principal stresses have also been observed at long (over several years) and short (few months) time scales at The Geysers geothermal field, where pore pressure conditions vary over time depending on the fluid injection scheme [*Martínez-Garzón et al.*, 2014a; *Kwiatek et al.*, 2015]. Such reported stress changes have not yet been clearly understood in terms of the underlying processes.

The stress inversion using earthquake focal mechanisms allows estimating the orientation of the principal stress axes and the stress ratio (also called the shape ratio or the relative stress magnitude) defined as

$$R = \frac{\sigma_1 - \sigma_2}{\sigma_1 - \sigma_3}. \quad (1)$$

Variations in R in relation to pore pressure, if detected, can have a physical origin but may also be spurious due to different inversion performance at different pore pressure levels. Technically, the stress inversion from focal mechanisms cannot retrieve the trace of the stress tensor. Therefore, the retrieved stress axes and R should be insensitive to pore pressure and its changes because pore pressure acts identically in all directions. However, the problem is more complicated, because the performance of the stress inversion under different pore pressure levels might be different. For example, a broader variety of fault planes is activated at high or low pore pressures, modifying thus how well sampled the possible fault orientations within a stress state are. As a consequence, pore pressure variations can affect the inverted stress tensor and, in particular, the stress ratio which is very sensitive to quality and extent of data and difficult to be retrieved accurately [e.g., *Vavryčuk*, 2015].

In this study, we investigate the effects of temporal pore pressure variations on the retrieved stress shape R using numerical modeling as well as field observations. We create a number of synthetic data sets, evaluate their fault plane variability, and study the effect of pore pressure on stress inversion results under three states of stress characterized by different imposed R. The results indicate that the retrieved stress ratio can display an apparent variation of substantial level under low average value of the shape ratio. These results are confirmed by findings from stress inversion applied to induced seismicity at The Geysers geothermal field in California.

2. Stress Tensor Inversion

Inversion of earthquake focal mechanisms to determine the stress orientation and the stress ratio is a well-established technique [e.g., *Angelier*, 1984; *Gephart and Forsyth*, 1984; *Michael*, 1984]. Here we apply the approach developed by *Michael* [1984, 1987] and adopted in the SATSI [*Hardebeck and Michael*, 2006] and MSATSI [*Martínez-Garzón et al.*, 2014b] software packages. These techniques are able to resolve spatio-temporal stress variations by performing a damped linear inversion applied to a set of focal mechanisms subdivided into subsets according to hypocenter locations and/or origin times.

Since the fault plane ambiguity in focal mechanisms may bias the retrieved stress ratio [*Vavryčuk*, 2015], the inversion is improved by incorporating an algorithm for identifying the fault plane from two nodal planes provided by a focal mechanism. The algorithm is based on evaluating the fault instability I [*Vavryčuk*, 2014]:

$$I = \frac{\tau + \mu(\sigma_n + 1)}{\mu + \sqrt{1 + \mu^2}}, \tag{2}$$

where τ and σ_n are the normalized shear and normal tractions and μ is the friction coefficient. Theoretically, the instability coefficient is independent of the pore pressure levels [*Vavryčuk et al.*, 2013]. For a number of iterations, the stress field is estimated and the correct fault planes are selected according to equation (2). Then, stress is inverted iteratively using these fault planes in a similar way as in the STRESSINVERSE code developed by *Vavryčuk* [2014].

3. Synthetic Stress and Focal Mechanisms

3.1. Stress Orientation

We generate several data sets of synthetic focal mechanisms to evaluate the resolution capability of stress ratio R under varying stress conditions. We perform three different tests (see section 4) in which we assume a normal faulting stress regime with stress axes defined by the following trend and plunge angles: S_1≡(200°, 80°), S_2≡(290°, 0.5°), and S_3≡(20°, 10°) and vary the stress ratio R^{synth}. The focal mechanisms are created using a normalized deviatoric stress tensor, and thus, no absolute stress magnitudes are needed. The imposed stress conditions do not completely match any specific environment. However, the second test is designed to approximate the conditions at the northwest part of The Geysers geothermal field [e.g., *Rutqvist et al.*, 2013; *Martínez-Garzón et al.*, 2014a], which is also the case study analyzed here (section 5).

3.2. Focal Mechanisms and Pore Pressure Variation

The temporal variation of the pore pressure is simulated by ordered series of 80 normalized pore pressure values expressing a pseudocyclic sequence imitating seasonal cycles of injection (Figure 2a). To generate the synthetic focal mechanisms in each subset, we create fault planes by randomly sampling the angles

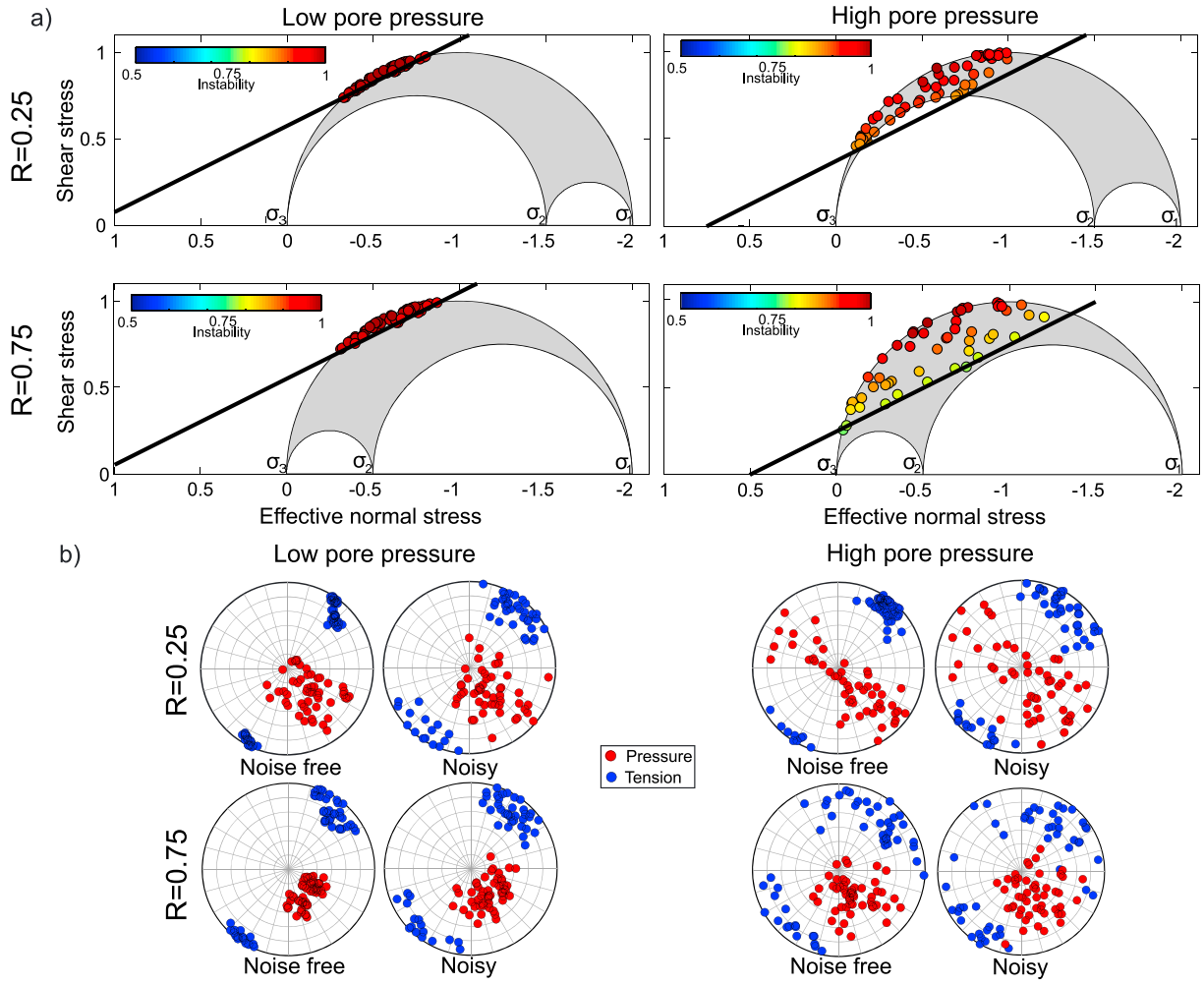

Figure 1. (a) Active fault planes in the Mohr diagram for low (left column) and high (right column) pore pressure levels and low (upper row) and high (lower row) stress ratios. Circle color is encoded with the fault instability [*Vavryčuk*, 2011]. (b) Examples of *P* and *T* axes distribution for noise-free and noisy focal mechanisms for the different conditions of pore pressure and stress ratios.

defining the fault geometry: strike $\phi = [0, 360]^\circ$ and dip $\delta = [0, 90]^\circ$ and select those satisfying the Mohr-Coulomb failure criterion:

$$\tau \geq S_0 + \mu(\sigma_n - P), \tag{3}$$

where S_0 is the rock cohesion, μ is the friction coefficient, and P the pore pressure. Rock cohesion is fixed to $S_0 \approx 0.2$ (i.e., 20% of the maximum shear traction in agreement with values estimated for fractured rocks) [*Zoback*, 2007]. The friction coefficient is set to $\mu = 0.5$ because of high extent of macrofracturing and presence of fluids in geothermal reservoirs. The corresponding rake angles are calculated according to the Wallace-Bott criterion stating that the slip on the fault occurs in the direction of the shear traction vector [*Wallace*, 1951; *Bott*, 1959].

In this way, we generate 4000 focal mechanisms and subdivide them into 80 subsets of 50 focal mechanisms. The stress state and pore pressure are fixed within each subset, but the pore pressure varies along the different subsets. As a consequence, the series of 80 subsets reflects time evolution of pore pressure and true stress ratio R^{synth}. If pore pressure increases, the subarea of the Mohr circle satisfying the failure criterion enlarges (e.g., Figure 1) and the orientations of activated fault planes extend over a broader range. By contrast, if pore pressure decreases, the scatter in orientations of activated fault planes decreases. We calculate the fault plane variability of each subset as the median of 3-D rotation angles [*Kagan*, 1991] between all focal mechanisms included in the subset.

Table 1. Correlation Coefficients of the Stress Inversions Performed in the Synthetic Tests

Test Number	R^{synth}	Noise (°)	Damping	Instability	Correlation	*p* Value
1	0,75	0	Yes	Yes	0,59	<0,001
1	0,75	0	No	Yes	0,47	<0,001
1	0,75	0	Yes	No	−0,08	0,47
1	0,75	20	Yes	Yes	−0,44	<0,001
1	0,75	20	No	Yes	−0,35	0,0015
1	0,75	20	Yes	No	0,82	<0,001
2	0,25	0	Yes	Yes	−0,97	<0,001
2	0,25	0	No	Yes	−0,95	<0,001
2	0,25	0	Yes	No	−0,26	0,0175
2	0,25	20	Yes	Yes	−0,93	<0,001
2	0,25	20	No	Yes	−0,88	<0,001
2	0,25	20	Yes	No	−0,90	<0,001
3a	[0,89–0,45]	0	Yes	Yes	−0,25	0,11
3a	[0,89–0,45]	0	No	Yes	−0,25	0,11
3a	[0,89–0,45]	0	Yes	No	−0,07	0,67
3a	[0,89–0,45]	20	Yes	Yes	−0,61	<0,001
3a	[0,89–0,45]	20	No	Yes	−0,59	<0,001
3a	[0,89–0,45]	20	Yes	No	−0,34	0,032
3b	[0,44–0]	0	Yes	Yes	−0,84	<0,001
3b	[0,44–0]	0	No	Yes	−0,87	0,150
3b	[0,44–0]	0	Yes	No	−0,23	0,15
3b	[0,44–0]	20	Yes	Yes	−0,90	<0,001
3b	[0,44–0]	20	No	Yes	−0,86	<0,001
3b	[0,44–0]	20	Yes	No	−0,89	<0,001

To simulate real situations, we take into account the ambiguity in choice of the fault from two nodal planes provided by focal mechanisms. We assume to have no a priori information about the orientation of true faults and run the stress inversion using fault planes randomly selected from the two nodal planes. The stress inversion algorithm works in iterations and jointly inverts for stress and fault orientations by maximizing the fault instability (equation (2)). The focal mechanisms in each data set are assumed to be noise free or with superimposed noise added to strike, dip, and rake angles reaching up to ±20°. Contaminating data by noise results in extending the fault planes along a larger portion of the Mohr circle beyond the failure criterion. Therefore, the effect could be similar to that of increasing the pore pressure. To test the sensitivity to the noisy conditions and obtain more representative results, we run the inversion of 100 noisy data sets and averaged them. Examples of the inverted stress ratio for individual noise realizations together with their stacked solution are shown in Figure S1 in the supporting information.

4. Synthetic Tests

We perform three synthetic tests evaluating the accuracy of the retrieved stress ratio R^{retr}. The imposed stress ratio was fixed: (1) constant at high value ($R = 0.75$), indicating a uniaxial stress state with $\sigma_1 > \sigma_2 \approx \sigma_3$; (2) constant at low value ($R = 0.25$), representing a mixed normal strike-slip faulting (transtensional) environment with $\sigma_1 = \sigma_V \approx \sigma_2 > \sigma_3$; and (3) linearly decreasing with time from $R = 0.9$ to $R = 0.1$. The decreased values may represent the evolution of a poroelastic reservoir under normal faulting stress subjected to long-term fluid injection, as observed, e.g., at the NW The Geysers geothermal field [e.g., *Segall and Fitzgerald*, 1998; *Altmann et al*., 2014; *Kwiatek et al*., 2015]. Alternatively, progressive decreasing of stress ratio in a normal faulting stress regime can represent an increase in σ_{HMAX} due to tectonic loading processes at an active plate-bounding fault [e.g., *Altmann et al*., 2013].

The tests are performed with noise-free and noisy focal mechanism data, with and without the iterative method identifying the most unstable fault planes (equation (2)) and with and without a damping factor. Correlation coefficients between pore pressure changes and stress ratio for each stress inversion distribution as well as *p* values from the Pearson distribution are provided in Table 1.

4.1. Test 1: Constant High Stress Ratio

The stress inversions of noise-free data reproduce correctly and accurately the imposed stress ratio (blue lines in Figure 2b). The best estimation is obtained when the fault instability criterion and the damped inversion

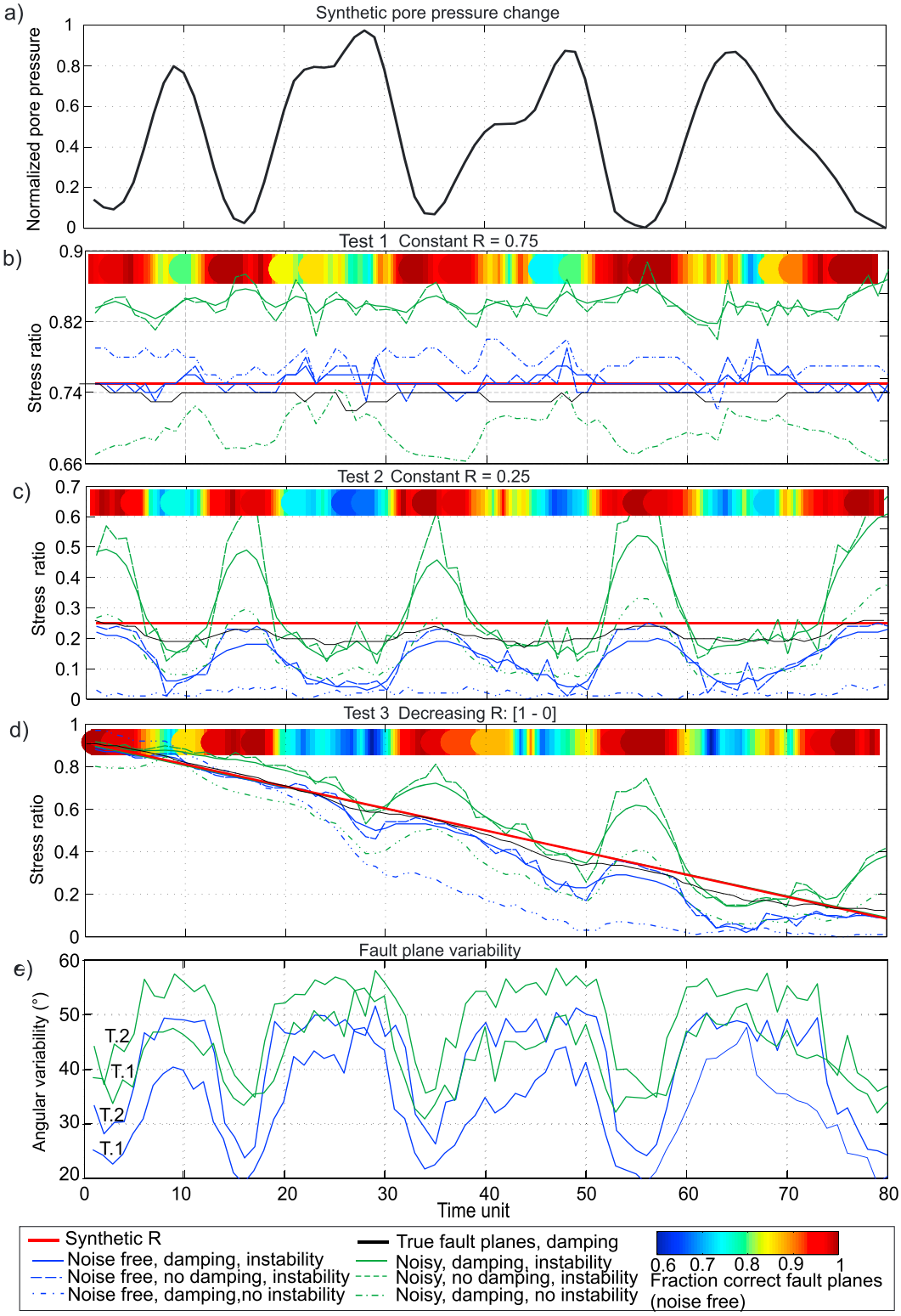

Figure 2. (a) Pore pressure variations in the three synthetic tests. (b–d) Time variations of the retrieved stress ratio in Test 1 (b), Test 2 (c), and Test 3 (d). Red line denotes the imposed stress ratio. Colorbar represents the fraction of correctly picked fault planes in each moving window. (e) Fault plane variability from subsets of noise-free (blue lines) and noisy (green lines) focal mechanism data for Tests 1 (T1) and 2 (T2).

scheme are applied. For noisy data, two different estimations are obtained: the inversions applying the fault instability criterion provide results by ~0.1 larger than the imposed R. However, if the fault instability criterion is not applied, the retrieved values are lower than the imposed R by ~0.07. Regardless of the noise conditions, no clear relation between pore pressure variation and the retrieved stress ratio is observed (Table 1 and Figure 2b). The fraction f_c of fault planes picked correctly using equation (2) from the initially random fault planes is near 1 during periods of low pore pressure, indicating that the algorithm is very effective in recovering of true fault planes. However, the effectiveness of the algorithm is observed to decrease during periods of increased pore pressure, down to approximately 0.75.

The fault plane variability at times of high pore pressure increases by about 20° with respect to periods of low pore pressure (Figure 2e). The distribution of P and T axes shows that the increased variability occurs preferentially in the T axes extending in the area between σ_2 and σ_3, which are horizontal in the normal faulting regime. Thus, the variation covers a range of azimuths (Figures 1c and 1d) at stable subhorizontal plunge.

4.2. Test 2: Constant Low Stress Ratio

When inverting noise-free data, the stress ratios retrieved using the fault instability criterion approach the exact imposed value only during the periods in which the normalized pore pressure is at its minimum. When pore pressure increases, the difference between imposed and resolved values of R increases (blue lines, Figure 2c). Therefore, a negative correlation between variations of R^{retr} and pore pressure is observed. During periods of low pore pressure, the instability algorithm picks the correct fault planes as effectively as for $R = 0.75$. However, the performance is lowered during high pore pressure down to nearly ≈ 65%. Choosing the fault plane randomly, the bias in the retrieved values of R^{retr} increases regardless of the pore pressure level, but no correlation between R^{retr} and pore pressure is observed (Table 1).

The inversion of noisy data at low pore pressure using the fault instability criterion provides biased estimation of R^{retr} that is larger by ~0.25 and ~0.4 than the imposed value for the damped and undamped inversions, respectively (green lines, Figure 2c). Moreover, the R^{retr} distributions display large variations which correlate with pore pressure changes. These variations are more pronounced when the fault instability criterion is applied.

Examples of focal mechanisms created under the same stress field orientation but with different pore pressure levels reflect a different distribution of the P and T axes on the focal sphere (Figure 1). During periods of high pore pressure, the plunges of the P axis cover the whole range from 0° to 90° (Figure 1b). The fault plane variability is larger by about 20° for high pore pressure than for low pore pressure, indicating a larger variability of focal mechanisms during those periods. The variability of the P and T axes between noise-free and noisy data varies from being nearly equal for high pore pressure to differ up to 20° for low pore pressure.

Even though the overall fault plane variability is slightly lower in Test 1 than in Test 2 (Figure 2e), the stress inversion performs better in Test 1. Comparison of the performance from Tests 1 and 2 suggests that the robustness and accuracy of the stress inversion is not a simple function of the fault plane variability, but it may depend on additional factors, such as the performance of the fault-choice criterion at different pore pressure levels.

4.3. Test 3: Linearly Decreasing Stress Ratio

This test shows that a temporally varying stress ratio can also be recovered reasonably well with the accuracy depending on the input data and the inversion scheme. The results are consistent with both tests previously performed. When $R > 0.6$, stress ratio R^{retr} is retrieved accurately from noise-free data regardless of pore pressure levels. Starting at $R \sim 0.6$, the values of R^{retr} display apparent variations which negatively correlate with pore pressure changes. When a random fault plane choice is performed, no clear correlation with pore pressure is observed, but the overall values of R^{retr} are less accurate. As in Test 2, if noise-free data are inverted, R^{retr} is accurate for periods of low pore pressure, but it deviates from true values when the pore pressure increases (blue lines in Figure 2d). In this test, the fraction of correctly picked fault planes decreases to approximately 0.65 during periods of high pore pressure regardless of the overall value of R. The values of R^{retr} display a more remarkable correlation using noisy data (green lines in Figure 2d), regardless of the stress inversion performed.

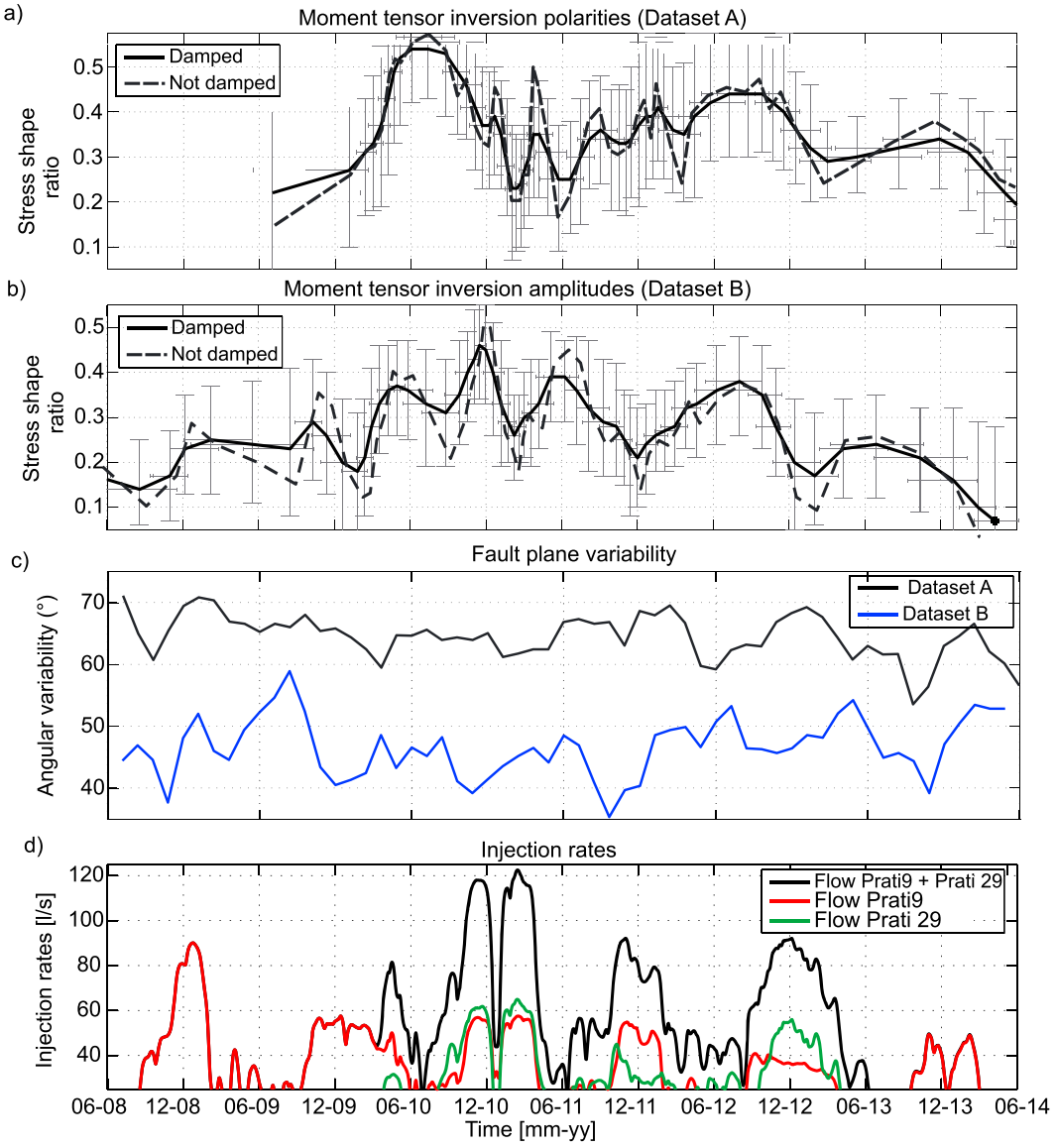

Figure 3. Stress ratios retrieved from focal mechanisms at The Geysers geothermal field. (a) Data set A. (b) Data set B. Inversions are performed using the instability criterion [*Vavryčuk*, 2014]. Vertical grey error bars mark the 95% confidence intervals for the damped scheme. (c) Focal mechanism variability as a function of time for data sets A (black) and B (blue). (d) Injection rates from the nearby wells and aggregated injection.

5. Case Study: Correlation Between Stress Ratio and Injection Rates at The Geysers Geothermal Field

To test the relation between the stress ratio and pore pressure changes using real focal mechanisms, we analyze the temporal evolution of the stress ratio at the NW part of The Geysers geothermal field. The overall stress regime in this area is normal faulting with a subvertical maximum compressive stress S_1 [*Martínez-Garzón et al.*, 2013]. The site is characterized by two wells which were injecting fluid at similar rates: the Prati-9 well, in operation since November 2007, and the Prati-29 well, only used for injection between 2010 and 2013 (Figure 3d). The injections show seasonal variations, with larger volumes injected in winter than in summer. In the vicinity of these wells, no steam production was performed until 2012. After 2012, three wells started production nearby, but the production volume remains significantly smaller than injection volume [cf. *Kwiatek et al.*, 2015]. Although reservoir pressure depends also on the rock properties and the diffusion of fluid/steam across the reservoir, the fluid injection is expected to govern the local pore pressure

around the wells. Additional support is provided by the injectivity test from the well Prati-9, where the borehole pressure was observed to increase by few MPa during peak injections [*Martínez-Garzón et al*., 2014b]. Therefore, fluid injection rates from these two wells are used as the first-order indicator of reservoir pore pressure, which is expected to change similarly as in the synthetic tests.

We create two data sets (A and B) of focal mechanisms using the local seismic network Berkeley-Geysers and a 1-D velocity model [*Eberhart-Phillips and Oppenheimer*, 1984]. Data set A contains 620 focal mechanisms obtained from first-motion polarities using HASH [*Hardebeck and Shearer*, 2002] software. Data set B is composed of 680 moment tensors constrained to represent a double-couple source estimated from *P* wave polarities and amplitudes using the hybridMT software [*Kwiatek et al*., 2016]. In addition, moment tensors from data set B were manually revised to detect potential wrong polarities. Thus, data set B is of higher accuracy than data set A. The focal mechanism variability of data set B is smaller than for data set A, indicating that the higher accuracy may have resulted in a significant reduction of the noise included in the focal mechanisms (Figure 3c). Focal mechanisms were sorted according to origin time and grouped into bins containing 25 events with an overlap of 10 events. Then, we invert for the stress field orientation and stress ratio as described in section 2. We used the instability criterion for selecting the fault planes, and both damped and undamped inversion schemes were tested.

The overall stress ratios are similar for both data sets (Figures 3a and 3b). Since the data sets do not contain the same number of events, the individual inversions do not match one to one. Data set A shows a decreasing stress ratio from $R^{retr} \approx 0.4$ to $R^{retr} \approx 0.3$ after a long-term injection. Data set B shows a rather constant average stress ratio of $R^{retr} \approx 0.3$. Temporal evolution of the stress ratio is different for each data set. The observed changes in R^{retr} using data set A are roughly negatively correlated with the overall evolution of the injection rates. This effect is enhanced when damping is not used thus allowing for faster changes in the stress ratio (Figures 3a and 3d). However, the changes in the injection rates are better resembled using focal mechanism derived from refined moment tensors from data set B (Figure 3b). This highlights the sensitivity of the retrieved stress ratio to the quality of input data. The results for the zero damping factor resemble more prominently the negative correlation between pore pressure and stress ratio found from synthetic tests. This is expected, since the damped stress approach is designed to minimize the stress changes from adjacent inversions. We interpolate the obtained curves to increase the sampling rate and divide the *R* distributions into four portions of equal size. Within these four windows, the correlation coefficients between the damped *R* distribution from data set B decrease in absolute value from -0.6 to -0.35, indicating that the correlation between *R* and injection rates is lowering with time.

6. Discussion and Conclusions

The results of the synthetic tests indicate that the retrieved stress ratio is sensitive to the stress inversion technique, the choice of the faults from the nodal planes, and the variability of focal mechanisms in the input data. If the three principal stresses are equally affected by pore pressure (i.e., if pore pressure is isotropic), the retrieved stress ratio should be theoretically independent of the pore pressure. However, synthetic tests suggest that pore pressure variations can easily cause apparent variations in the stress ratio. This is confirmed by analyzing induced seismicity recorded at The Geysers geothermal field and comparing the temporal evolution of the stress ratio with the injection rates of the local wells.

Both synthetic tests and field observations indicate that the apparent variations of the stress ratio and the pore pressure variations are negatively correlated if the overall stress ratio is low. For a high stress ratio, the apparent variations in the retrieved value R^{retr} are mostly suppressed. This might have several origins. One possibility influencing the accuracy of the stress inversion is the decreased performance of the algorithm to pick the correct fault plane during time periods of high injection rates may result in deviating the retrieved R^{retr} from the correct value. Picking the correct fault plane has been observed to play an important role for the estimation of *R* [*Vavryčuk*, 2014; 2015]. However, this cannot be the only reason for the observed correlation because (a) decreased performance is also observed with high *R* and high pore pressure but no apparent variations in R^{retr} are observed and (b) stress inversions using noise-free data and correct fault planes are more accurate but they also suggest this dependence (see Figure 2, black lines). Other possibilities are related to the variability in the orientation of the activated fault planes. The variability in fault orientations is low for high values of *R* (see Figure 2e, blue line for T1); hence, it is sufficient to invert a low number of focal mechanisms

to get a reliable stress ratio R^{retr}. By contrast, the variability in fault orientations is high for low values of R (see Figure 2e, blue line for T2); thus, a high number of focal mechanisms is needed to sample densely activated faults and to get a sufficiently accurate stress ratio R^{retr}. In addition, the variability in fault orientations increases with pore pressure. Consequently, increasing pore pressure decreases the accuracy of the retrieved R^{retr} (see Figure 2c, blue lines). When inverting noisy data, the problem is even more involved (see Figure 2c, green lines).

Based on the correlation coefficients between pore pressure and the retrieved stress ratio (cf. Table 1), the optimum technique to get both overall stress ratio and pore pressure variation (if they can be recovered) is to use a stress inversion which combines the instability criterion for selecting the fault [*Vavryčuk*, 2014] and the damped inversion scheme [*Hardebeck and Michael*, 2006]. However, we suggest to perform and compare the results with different stress inversion schemes to determine the robustness of the obtained R^{retr} distribution.

We also investigated whether the relation between the stress ratio and pore pressure observed under a normal faulting environment still holds in other faulting environments. We performed additional tests using equivalent initial conditions as in the synthetic cases under normal faulting by interchanging the principal stress axes to represent strike-slip and reverse fault styles (Figure S2). Both noise-free and noisy data were used, and the inversion was performed using a damped inversion and including the fault plane instability criterion. In these tests, the negative correlation between stress ratio and pore pressure changes is found for both noise-free and noisy data in both stress environments with $R = 0.25$. Interestingly, weak positive correlations are also found using noisy data with $R = 0.75$ under strike-slip and reverse faulting, which were not observed under normal faulting environment.

We focused on studying the relation between the retrieved stress ratio and pore pressure variations under assumption of time independent orientation of the stress axes. However, other more complex situations may also occur. For example, the change in the stress ratio can be accompanied by a rotation of the corresponding stress axes. Preliminary results based on similar tests including a temporally varying stress do not seem to significantly affect the retrieved stress ratios. However, a more complete description of how stress rotations may affect the retrieved stress values remains not addressed.

To avoid including additional assumptions on stress magnitudes, we have worked with the deviatoric stress components retrieved from the stress inversion. Assuming absolute stress values, we can infer the magnitude of the pore pressure changes simulated here. For the environment at The Geysers geothermal field at ~2.8 km depth, the stress magnitudes may be approximated according to the rock parameters as $\sigma_1 = 74$ MPa, $\sigma_2 = 60$ MPa, and $\sigma_3 = 24$ MPa (Martinez-Garzon et al., in review). Using these parameters, the simulated pore pressure variation (section 4) would be up to $\Delta P \approx 11$ MPa (i.e., ≈15% of σ_1), which is a realistic value for many fluid injection experiments. Therefore, in stress environments displaying an overall low stress ratio (e.g., transtensional environments), the stress ratio can serve as an additional tool for verifying or even monitoring pore pressure changes at local scale (e.g., reservoir characterization) or even regional scale.

Acknowledgments
We acknowledge funding from the Helmholtz Association (P.M.G. and M.B.), Grant Agency of Czech Republic, projects P210/12/1491 and 16-19751 J (VV). We thank the Editor M. Bayani Cardenas, Andrew Barbour, and two anonymous reviewers for their useful reviews. Data presented here can be provided under request at patricia@gfz-potsdam.de.

References

Altmann, J., O. Heidbach, and R. Gritto (2013), Relative importance of processes leading to stress changes in the Geysers geothermal area, *Proc. Thirty-Eight Workshop Geotherm. Reserv. Eng. Stanford Univ.*, Stanford, Calif., 11-13 Feb.

Altmann, J. B., B. I. R. Müller, T. M. Müller, O. Heidbach, M. R. P. Tingay, and A. Weißhardt (2014), Pore pressure stress coupling in 3D and consequences for reservoir stress states and fault reactivation, *Geothermics*, *52*, 195–205, doi:10.1016/j.geothermics.2014.01.004.

Angelier, J. (1984), Tectonic analysis of fault slip data sets, *J. Geophys. Res.*, *89*(B7), 5835–5848, doi:10.1029/JB089iB07p05835.

Barbour, A. J. (2015), Pore pressure sensitivities to dynamic strains: Observations in active tectonic regions, *J. Geophys. Res. Solid Earth*, *120*, 5863–5883, doi:10.1002/2015JB012201.

Bohnhoff, M., S. Baisch, and H.-P. Harjes (2004), Fault mechanisms of induced seismicity at the superdeep German Continental Deep Drilling Program (KTB) borehole and their relation to fault structure and stress field, *J. Geophys. Res.*, *109*, L01309, doi:10.1029/2003JB002528.

Bott, M. H. P. (1959), The mechanics of oblique slip faulting, *Geol. Mag.*, *96*, 109–117.

Brudy, M., M. D. Zoback, K. Fuchs, F. Rummel, and J. Baumgärtner (1997), Estimation of the complete stress tensor to 8 km depth in the KTB scientific drill holes: Implications for crustal strength, *J. Geophys. Res.*, *102*(B8), 18,453–18,475, doi:10.1029/96JB02942.

Eberhart-Phillips, D., and D. H. Oppenheimer (1984), Induced seismicity in The Geysers Geothermal Area, California, *J, Geophys. Res.*, *89*(B2), 1191–1207, doi:10.1029/JB089iB02p01191.

Gephart, J. W., and D. W. Forsyth (1984), An improved method for determining the regional stress tensor using earthquake focal mechanism data: Application to the San Fernando earthquake sequence, *J. Geophys. Res.*, *89*(B11), 9305–9320, doi:10.1029/JB089iB11p09305.

Hardebeck, J. L., and E. Hauksson (1999), Role of fluids in faulting inferred from stress field signatures, *Science*, *285*(5425), 236–239, doi:10.1126/science.285.5425.236.
Hardebeck, J. L., and E. Hauksson (2001), Stress orientations obtained from earthquake focal mechanisms: What are appropriate uncertainty estimates?, *Bull. Seismol. Soc. Am.*, *91*(2), 250–262, doi:10.1785/0120000032.
Hardebeck, J. L., and A. J. Michael (2006), Damped regional-scale stress inversions: Methodology and examples for southern California and the Coalinga aftershock sequence, *J. Geophys. Res.*, *111*, B11310, doi:10.1029/2005JB004144.
Hardebeck, J. L., and P. M. Shearer (2002), A new method for determining first-motion focal mechanisms, *Bull. Seismol. Soc. Am.*, *92*(6), 2264–2276, doi:10.1785/0120010200.
Hickman, S., and M. Zoback (2004), Stress orientations and magnitudes in the SAFOD pilot hole, *Geophys. Res. Lett.*, *31*, L15S12, doi:10.1029/2004GL020043.
Kagan, Y. Y. (1991), 3-D rotation of double-couple earthquake sources, *Geophys. J. Int.*, *106*, 709–716.
Kwiatek, G., P. Martínez-Garzón, G. Dresen, M. Bohnhoff, H. Sone, and C. Hartline (2015), Effects of long-term fluid injection on induced seismicity parameters and maximum magnitude in northwestern part of The Geysers geothermal field, *J. Geophys. Res. Solid Earth*, 7085–7101, doi:10.1002/2015JB012362.
Kwiatek, G., P. Martínez-Garzón, and M. Bohnhoff (2016), HybridMT: A MATLAB/Shell environment package for seismic moment tensor inversion and refinement, *Seismol. Res. Lett.*, *87*(4), doi:10.1785/0220150251.
Martínez-Garzón, P., M. Bohnhoff, G. Kwiatek, and G. Dresen (2013), Stress tensor changes related to fluid injection at The Geysers geothermal field, California, *Geophys. Res. Lett.*, *40*, 2596–2691, doi:10.1002/grl.50438.
Martínez-Garzón, P., G. Kwiatek, H. Sone, M. Bohnhoff, G. Dresen, and C. Hartline (2014a), Spatiotemporal changes, faulting regimes, and source parameters of induced seismicity: A case study from The Geysers geothermal field, *J. Geophys. Res. Solid Earth*, *119*, 8378–8396, doi:10.1002/2014JB011385.
Martínez-Garzón, P., G. Kwiatek, M. Ickrath, and M. Bohnhoff (2014b), MSATSI: A MATLAB package for stress inversion combining solid classic methodology, a new simplified user-handling, and a visualization tool, *Seismol. Res. Lett.*, *85*(4), 896–904, doi:10.1785/0220130189.
Michael, A. J. (1984), Determination of stress from slip data: Faults and folds, *J. Geophys. Res.*, *89*(B13), 11,517–11,526, doi:10.1029/JB089iB13p11517.
Michael, A. J. (1987), Use of focal mechanisms to determine stress: A control study, *J. Geophys. Res.*, *92*(B1), 357–368, doi:10.1029/JB092iB01p00357.
Moreno, M., C. Haberland, O. Oncken, A. Rietbrock, S. Angiboust, and O. Heidbach (2014), Locking of the Chile subduction zone controlled by fluid pressure before the 2010 earthquake, *Nat. Geosci.*, *7*(4), 292–296, doi:10.1038/ngeo2102.
Rutqvist, J., P. F. Dobson, J. Garcia, C. Hartline, P. Jeanne, C. M. Oldenburg, D. W. Vasco, and M. Walters (2013), The northwest Geysers EGS demonstration project, California: Pre-stimulation modeling and interpretation of the stimulation, *Math. Geosci.*, *47*, 3–29, doi:10.1007/s11004-013-9493-y.
Schoenball, M., L. Dorbath, E. Gaucher, J. F. Wellmann, and T. Kohl (2014), Change of stress regime during geothermal reservoir stimulation, *Geophys. Res. Lett.*, *41*, 1163–1170, doi:10.1002/2013GL058514.
Segall, P., and S. D. Fitzgerald (1998), A note on induced stress changes in hydrocarbon and geothermal reservoirs, *Tectonophysics*, *289*(1–3), 117–128, doi:10.1016/S0040-1951(97)00311-9.
Terakawa, T., S. A. Miller, and N. Deichmann (2012), High fluid pressure and triggered earthquakes in the enhanced geothermal system in Basel, Switzerland, *J. Geophys. Res.*, *117*, B07305, doi:10.1029/2011JB008980.
Townend, J., and M. D. Zoback (2000), How faulting keeps the crust strong, *Geology*, *28*(5), 399–402.
Vavryčuk, V. (2011), Principal earthquakes: Theory and observations for the 2008 West Bohemia swarm, *Earth Planet. Sci. Lett.*, *305*(3–4), 290–296, doi:10.1016/j.epsl.2011.03.002.
Vavryčuk, V. (2014), Iterative joint inversion for stress and fault orientations from focal mechanisms, *Geophys. J. Int.*, *199*(1), 69–77, doi:10.1093/gji/ggu224.
Vavryčuk, V. (2015), Earthquake mechanisms and stress field, in *Encyclopedia of Earthquake Engineering*, edited by M. Beer et al., pp. 728–746, Springer, Berlin, doi:10.1007/978-3-642-36197-5_295-1.
Vavryčuk, V., F. Bouchaala, and T. Fischer (2013), High-resolution fault image from accurate locations and focal mechanisms of the 2008 swarm earthquakes in West Bohemia, Czech Republic, *Tectonophysics*, *590*, 189–195, doi:10.1016/j.tecto.2013.01.025.
Wallace, R. E. (1951), Geometry of shearing stress and relation to faulting, *J. Geol.*, *59*(2), 118–130.
Zoback, M. D. (2007), *Reservoir Geomechanics*, Cambridge Univ. Press, Cambridge.
Zoback, M. L. (1992), First- and second-order patterns of stress in the lithosphere: The World Stress Map Project, *J. Geophys. Res.*, *97*(B8), 11,703–11,728, doi:10.1029/92JB00132.